Solution-Processed MoS_2/Organolead Trihalide Perovskite Photodetectors

Yan Wang, Raymond Fullon, Muharrem Acerce, Christopher E. Petoukhoff, Jieun Yang, Chenggan Chen, Songnan Du, Sin Ki Lai, Shu Ping Lau, Damien Voiry, Deirdre O'Carroll, Gautam Gupta, Aditya D. Mohite, Shengdong Zhang, Hang Zhou, and Manish Chhowalla**

Integration of heterogeneous materials provides opportunities for achieving new types of electronic and optoelectronic devices with increased performance. 2D materials such as single or few-layered transition metal dichalcogenides (TMDs) exhibit interesting optical and electronic properties that are of fundamental and technological interest.[1] The integration of 2D materials with other low-dimensional materials such as single-walled carbon nanotubes[2] or PbS quantum dots[3] leads to substantial enhancement in the light absorption and quantum efficiency which in turn can substantially improve the responsivity of a photodetector.[4] Incorporation of 3D or molecular absorption layers such as amorphous silicon[5] and rhodamine 6G fluorescent dye[6] can also modify light matter interactions in 2D materials. Like 2D TMDs, organolead trihalide perovskites with the formula of $MAPbX_3$ (MA = methylammonium CH_3NH_3 and X = halogen) possess interesting optical and electronic properties such as long free carrier diffusion lengths and high absorption, which results in excellent solar cell performance.[7,8] The integration of lead halide perovskites with 2D TMDs and other layered materials, therefore, offers opportunities for studying unique charge transfer mechanisms and light matter interactions in devices such as photodetectors. To this end, perovskites have been integrated as absorption layers on graphene,[9–11] reduced graphene oxide,[12] MoS_2,[13] WS_2,[14] and WSe_2[15] to improve photoresponsivitiy in photodetectors. A key challenge in integrated perovskite/2D material photodetectors is the need to improve the photoresponsivity while maintaining a low dark state current. That is for a highly conducting 2D layer such as graphene, substantial current is present in the dark (or off) state and the relative enhancement in the photo (or on state) current is low and therefore the overall on/off ratio is impractical. Furthermore, most high responsivity photodetectors utilize 2D layers that are deposited by either chemical vapor deposition or mechanical exfoliation.[16–18] Large area solution based deposition of high-quality chemically exfoliated 2D materials could provide ease of fabrication and allow many integrated devices over large areas to be tested.

In this study, we have fabricated solution-processed heterostructures consisting of 2D MoS_2 and perovskite with device structure illustrated in **Figure 1**a for photodetection. Bulk MoS_2 powder was chemically exfoliated, using the well-established lithium intercalation method, into monolayer nanosheets that are soluble in water.[19] We have reported the detailed characterization of 2D chemically exfoliated MoS_2 nanosheets elsewhere in several published reports.[19–21] The nanosheets fabricated here were characterized with Raman and X-ray photoelectron spectroscopies (XPS) to obtain the concentration of the metallic and semiconducting phases. Uniform deposition of MoS_2 nanosheets was carried out using vacuum filtration and transfer onto the target substrate.[19,22] It is well known that 2D MoS_2 can exist in either the semiconducting trigonal prismatic (2H phase) or the metallic octahedral (1T phase) crystal structures.[23] Chemical exfoliation of bulk MoS_2 using lithium intercalation leads to nanosheets that are primarily 1T phase and therefore electrically conducting.[24] The 1T phase of MoS_2 is metastable and can be relaxed to the thermodynamically stable 2H-MoS_2 phase by annealing at 300 °C in vacuum or argon for 2 h.[19] The 1T phase concentration in the exfoliated nanosheets is ≈70% at room temperature but decreases to 0% (or 100% 2H phase) after annealing at 300 °C.

The thickness of the solution processed thin films of MoS_2 nanosheets can be precisely controlled by vacuum filtration. We have systematically investigated the effect of the MoS_2 thickness and phase on the performance of the photodetectors. We fabricated devices using three thicknesses of 1T and 2H phase MoS_2 nanosheets while keeping the thickness of the perovskite film constant. The thicknesses of MoS_2 nanosheet films correspond to an electrically percolating but not fully continuous layer

Y. Wang, R. Fullon, Dr. M. Acerce, C. E. Petoukhoff, Dr. J. Yang, Dr. D. Voiry, Prof. D. O'Carroll, Prof. M. Chhowalla
Materials Science and Engineering
Rutgers University
607 Taylor Road, Piscataway, NJ 08854, USA
E-mail: manish1@rci.rutgers.edu

Y. Wang, C. Chen, S. Du, Prof. S. Zhang, Prof. H. Zhou
Shenzhen Key Lab of Thin Film Transistor and Advanced Display
Peking University Shenzhen Graduate School
Peking University
Shenzhen 518055, China
E-mail: zhouh81@pkusz.edu.cn

S. K. Lai, Prof. S. P. Lau
Department of Applied Physics
The Hong Kong Polytechnic University
Hung Hom, Kowloon HKSAR, Hong Kong, P. R. China

Prof. G. Gupta, Dr. A. D. Mohite
MPA-11 Materials Synthesis and Integrated Devices
Los Alamos National Laboratory
Los Alamos, NM 87545, USA

DOI: 10.1002/adma.201603995

ADVANCED MATERIALS
www.advmat.de

www.MaterialsViews.com

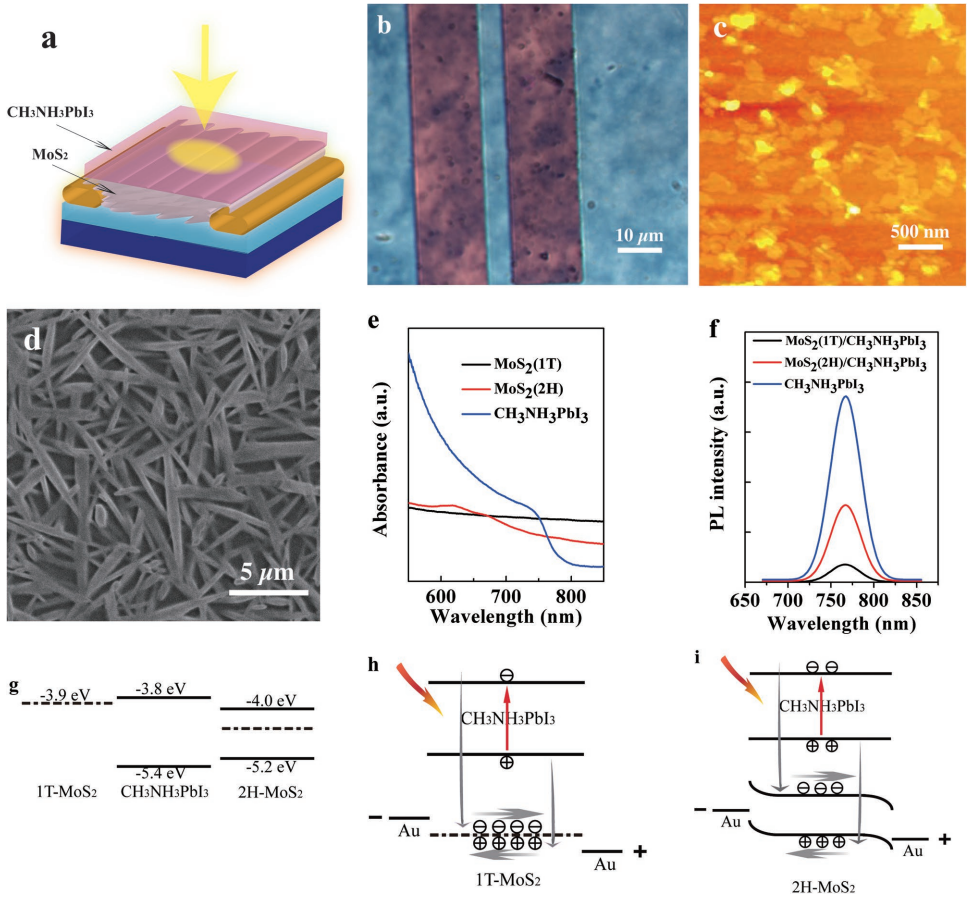

Figure 1. a) Schematic of the photodetection device. b) Optical microscopy image showing MoS_2 channels (blue regions) and gold electrodes (pink regions). c) AFM image of MoS_2 sheets in the thinnest film showing a percolating but not continuous film. d) Typical scanning electron microscope (SEM) image of perovskite films on MoS_2 nanosheets. e) UV–vis absorption spectra of pristine MoS_2 and $CH_3NH_3PbI_3$ films. f) PL spectra of pristine $CH_3NH_3PbI_3$ and hybrid $MoS_2/CH_3NH_3PbI_3$ thin films upon excitation at 532 nm. g) Energy band diagram of 1T and 2H phases of MoS_2 and perovskite. The energy levels were determined using Kelvin probe force microscopy (KPFM). The dotted lines represent the Fermi levels of the MoS_2. h) Working mechanism of 1T-$MoS_2/CH_3NH_3PbI_3$ photodetector. i) Working mechanism of 2H-$MoS_2/CH_3NH_3PbI_3$ photodetector.

(≈80% coverage of the channel surface), completely continuous channel film with full coverage, and thick multi-layered film. An optical microscopy image of the device with continuous MoS_2 film is shown in Figure 1b; the blue area is MoS_2 film deposited on silicon oxide and the pink rectangles indicate patterned gold electrodes. Optical images of different thicknesses of MoS_2 are given in Figure S1 (Supporting Information). A corresponding atomic force microscope (AFM) image showing 2D MoS_2 sheets in the thinnest film is shown in Figure 1c. The surface morphology of perovskite thin films deposited using a simple one-step spin-coating method is shown in Figure 1d. The fibril-like network morphology of the perovskite thin film on MoS_2 is similar to that on SiO_2, as shown in our previous report.[25] Planar structure perovskite photodetectors employing this method provide advantages of uniformity, photosensitivity, and flexibility.

To investigate the optical properties of the hybrid $MoS_2/CH_3NH_3PbI_3$ films, UV–vis and steady-state photoluminescence (PL) spectroscopy measurements were conducted. UV–vis absorption results of pristine MoS_2 films (1T and 2H phases) and pristine $CH_3NH_3PbI_3$ film are presented in Figure 1e. MoS_2 films deposited from nanosheets exfoliated by lihtium chemistry exhibit no obvious absorption peaks due to their high 1T phase concentration, rendering them metallic. In contrast, annealed MoS_2 films that are semiconducting 2H phase show typical peaks between 600 and 700 nm that can be attributed to A and B excitons arising from the K point of the Brillouin zone.[26] Absorption of pristine perovskite film shows an obvious absorption edge around 760 nm corresponding to its direct optical bandgap.[27] We have also illustrated absorption for pristine MoS_2 films of different thicknesses and a hybrid $MoS_2/CH_3NH_3PbI_3$ film in Figure S2 (Supporting Information). After deposition of the perovskite layer, the two absorption peaks of 2H-MoS_2 remain visible. To further confirm the phase of MoS_2, we conducted Raman and XPS spectroscopies on pristine MoS_2 films (Figures S3 and S4, Supporting Information). Two prominent peaks corresponding to the in-plane E^1_{2g} (382 cm^{-1}) and out-of-plane A_{1g} (405 cm^{-1}) modes of 2H-MoS_2 can be seen clearly. Chemically exfoliated samples exhibit weak peaks in the lower frequency region, referred to as J1, J2, and J3, that correspond to modes that are active in 1T-MoS_2.[28] The two samples of MoS_2 were identified by XPS

DOI: 10.1002/adma.201603995

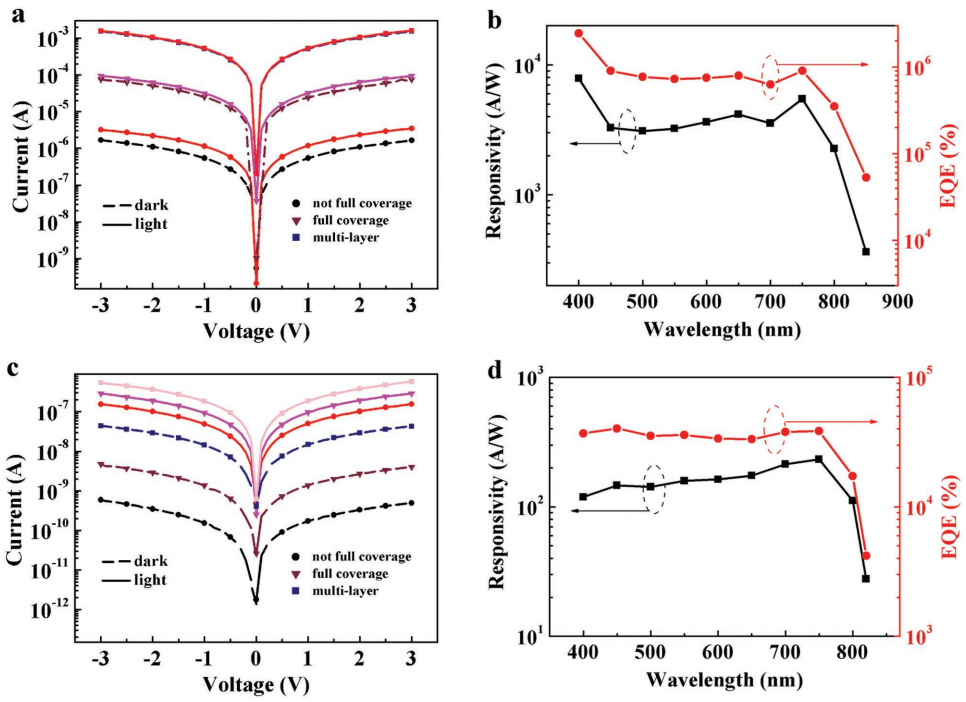

Figure 2. a) *I–V* curves of 1T-MoS_2/$CH_3NH_3PbI_3$ in dark and white light with different thicknesses of MoS_2. b) Responsivity and EQE results of 1T-MoS_2/$CH_3NH_3PbI_3$ photodetector. The results are for the thinnest 1T phase MoS_2 films. c) *I–V* curves of 2H-MoS_2/$CH_3NH_3PbI_3$ in dark and white light with different thicknesses of MoS_2. d) Responsivity and EQE results of multi-layered 2H-MoS_2/$CH_3NH_3PbI_3$ photodetector.

in Mo 3d, S 2s, and S 2p regions. It has been confirmed that the peaks from the 1T phase appear at a binding energy that is ≈0.9 eV lower than the 2H phase.[29] Figure 1g shows the PL spectra of the $CH_3NH_3PbI_3$ and MoS_2/$CH_3NH_3PbI_3$ samples prepared under the same conditions. As we can see from the figure, both samples exhibit PL at ≈767 nm arising from the bandgap of perovskite (≈1.6 eV), which can be attributed to band-to-band recombination.[30,31] However, a dramatic quenching was observed for both 1T-MoS_2/$CH_3NH_3PbI_3$ and 2H-MoS_2/$CH_3NH_3PbI_3$ hybrid films. Specifically, the peak intensity of hybrid 2H-MoS_2/$CH_3NH_3PbI_3$ was quenched by ≈60% with respect to the peak intensity of the pure perovskite film, resulting from injection of electrons and holes from the perovskite to 2H-MoS_2.[13] Moreover, the peak intensity of hybrid 1T-MoS_2/$CH_3NH_3PbI_3$ was quenched by ≈90%, indicating more effective charge transfer from perovskite to 1T-MoS_2. In addition, we observed higher quenching for films with continuous coverage and multi-layered MoS_2.

PL quenching in hybrid MoS_2/$CH_3NH_3PbI_3$ occurs due to injection of photogenerated electrons and/or holes from perovskite into MoS_2. It has recently been shown that MoS_2 can be used as a hole transport layer in perovskite solar cells.[32] To understand how photogenerated carriers are transferred from the perovskites into MoS_2, we consider the energy band alignment of the different layers. Energy band diagrams of MoS_2/$CH_3NH_3PbI_3$ are given in Figure 1g and the charge transfer mechanisms in the 1T and 2H phase MoS_2 are shown in Figure 1h,i, respectively. We previously measured the Fermi level position of the 1T phase MoS_2 by Kelvin probe force microscopy (KPFM) and found that it is located near the conduction band energy of the 2H phase MoS_2.[33] Thus, based on the energy band diagram in Figure 1g, it can be seen from Figure 1h that upon application of an electric field between the MoS_2 electrodes, photogenerated electrons and holes can be injected into the metallic 1T phase MoS_2. The injection of both types of carriers likely leads to recombination of carriers in 1T phase MoS_2, which would decrease the performance of the devices. However, since the current in the metallic 1T phase MoS_2 is approximately two orders of magnitude higher than in the 2H phase devices (**Figure 2**), higher responsivity with low on/off ratios are observed. The charge transfer mechanism in the 2H-MoS_2/$CH_3NH_3PbI_3$ devices is shown in Figure 1i. Specifically, the photogenerated electrons and holes from the perovskite are injected into the conduction and valence bands of the 2H phase MoS_2, respectively. The presence of the Schottky barrier at the contacts allows electrons and holes to be collected at the respective electrodes.[13]

The efficient charge transfer from perovskite to MoS_2 indicated by the PL quenching suggests that the MoS_2/$CH_3NH_3PbI_3$ heterostructure photodetectors should exhibit good photoresponse. The current–voltage curves of 1T-MoS_2/$CH_3NH_3PbI_3$ devices under dark and 100 mW cm^{-2} white light illumination with different thicknesses of MoS_2 films are shown in Figure 2a. The typical linear and symmetrical plots of dark current and photocurrent versus voltage indicate that hybrid 1T-MoS_2/$CH_3NH_3PbI_3$ form low resistance contacts with the gold electrodes. The dark current of the device increases almost three orders with increasing thickness of MoS_2. Since $I = J\,S = \sigma ES = nq\mu EWd$ (where n is the concentration of carriers, q is the absolute value of electron charge (1.6×10^{-19} Coulombs), μ is the mobility, E is the applied electric field, W is the channel width, and d is the film thickness), the increase

in dark current with thickness is likely due to an increase in the equivalent mobility or the concentration of carriers, which could result from the evolution of the band structure of MoS_2 from single- to multi-layers. Owing to the more efficient charge collection, the resulting photocurrent ($I_{ph} = I_{illuminated} - I_{dark}$) also increases with increasing thickness of MoS_2 at the same bias voltage. The responsivity and external quantum efficiency (EQE) of devices with the thinnest MoS_2 films are illustrated in Figure 2b under illumination wavelengths between 400 and 850 nm and bias of 2 V. The responsivity (R) of a photodetector is defined as $\frac{I_{ph}}{P}$, where I_{ph} and P are the photocurrent density (mA cm^{-2}) and incident illumination power density (mW cm^{-2}), respectively. The EQE of a photodetector can be calculated by EQE = $R\ E \times 100$, where R and E are the responsivity (A W^{-1}) and the incident photon energy (J), respectively. As the wavelength increases, there is an obvious decline for both responsivity and EQE above 770 nm which is attributed to the excitation of charges in the perovskite layer. An enhancement in the 1T-MoS_2 device under 400 nm light exposure can be seen in Figure 2b but a similar upward trend is not observed in the 2H-MoS_2 devices (Figure 2d). We attribute this to the fact that the perovskite layer completely absorbs the radiation at 400 nm, leading to a substantial increase in the concentration of photogenerated charge carriers. The 1T phase is able to accommodate the injection of higher concentration of carriers due to its metallic nature—leading to a significant enhancement in the photoresponsivity. In contrast, the semiconducting nature of the 2H phase creates a bottleneck for injection of carriers—thus a substantial increase in performance is not observed at 400 nm.

At a light power density of 37.9 μW cm^{-2} and a wavelength of 500 nm, the 1T phase hybrid photodetector exhibits a responsivity of 3096 A W^{-1} and an EQE of 7.7 × 10^5%, which is comparable to CVD (Chemical Vaport Deposition)-processed graphene and (MoS_2,WS_2)/perovskite hybrids[9,10,13,14,34] and single crystal perovskite photodetectors.[35,36] It is worth noting that with multi-layered 1T-MoS_2 film hybrid photodetector, we obtain even higher responsivity and EQE. However, the on/off ratio of the 1T-MoS_2/$CH_3NH_3PbI_3$ is limited by the high dark current, as also observed in the case of graphene/$CH_3NH_3PbI_3$ photodetectors.[9–11,34,37] This is attributed to the high conductivity of graphene, and in our case metallic 1T-MoS_2. As seen from Figure 2a, the on/off ratios are all lower than 2, which make such photodetectors impractical for integrated circuit devices, despite their exceptionally high responsivity.

To address the on/off ratio, we investigated devices using 2H phase MoS_2 nanosheets. The current–voltage curves of 2H-MoS_2/$CH_3NH_3PbI_3$ heterostructure devices under dark and 100 mW cm^{-2} white light illumination with different thickness of MoS_2 films are presented in Figure 2c. Similar to the 1T phase MoS_2 devices, the linear and symmetrical dark current and photocurrent versus voltage show that the contacts are low resistance. The dark current of the device increases with increasing thickness of MoS_2. More significantly, however, the on/off ratio increases significantly relative to the metallic 1T phase MoS_2 devices, reaching a value of ≈300. Our results demonstrate that there is a compromise between responsivity and on/off ratio in the performance of the hybrid photodetectors. The responsivity and EQE results of the multi-layered 2H phase MoS_2 devices are illustrated in Figure 2d under different illumination wavelengths at a bias of 2 V. At a light power intensity of 31.3 μW cm^{-2} at 500 nm wavelength, the multi-layered 2H phase hybrid photodetector exhibits a responsivity of 142 A W^{-1} and an EQE of 3.5 × 10^4%, which is much better than CVD-deposited monolayer MoS_2 phototransistors[38] and pure perovskite film photodetectors.[39–41]

We have also explored photoresponsivity dependence of both hybrid structures on light intensity. The current–voltage curves of 1T-MoS_2/$CH_3NH_3PbI_3$ and 2H-MoS_2/$CH_3NH_3PbI_3$ photodetectors under 500 nm illumination at power ranging from 0.14 to 13.27 μW are shown in **Figure 3**a,c, respectively. From these curves, we can see that the photocurrent of both structures rises with the increasing illumination light power. We also observe this rising trend when considering the responsivities at different thickness of MoS_2 as a function of illumination power, as summarized in Figure 3b,d for the 1T and 2H phases, respectively. As a result, we can obtain a responsivity of 3.3 × 10^5 A W^{-1} for multi-layered 1T-MoS_2/$CH_3NH_3PbI_3$ devices at a power of 0.14 μW, the highest value measured in this study. The increase in photoresponsivity can be attributed to higher conductivity of the thicker MoS_2 films. As we see from the current voltage measurements, the dark current increases with thickness—suggesting that the conductivity of both types of MoS_2 increases with thickness. Higher conductivity should lead to increase in charge transfer and transport, which will lead to an enhancement in the photoresponsivity.

Another important parameter of a photodetector is photodetectivity (D^*), which is defined as $\frac{(A\Delta f)^{\frac{1}{2}}R}{i_n}$ where A is the working area of the device, Δf is the electrical bandwith, and i_n is the noise current. If, as expected, the shot noise from the dark current is the major contribution, the detectivity can be expressed as $R\left(\frac{A}{2qI_d}\right)^{1/2}$ where q is the absolute value of electron charge (1.6 × 10^{-19} Coulombs) and I_d is the dark current. The detectivities of multi-layered 1T-MoS_2/$CH_3NH_3PbI_3$ devices and 2H-MoS_2/$CH_3NH_3PbI_3$ devices are shown in Figure 3b,d. Owing to the enhanced responsivity, D^* was found to exceed 10^{11} Jones at 0.14 μW - specifically, 7 × 10^{11} Jones was measured for the 1T phase multi-layered devices and 2.6 × 10^{11} Jones for 2H devices. The detectivity we obtained is better than that reported for heterostructure graphene/perovskite photodetectors. Importantly, we can adjust the phase and thickness of MoS_2 to gain better performance of the detectors by this solution process method. Detailed performance parameters of reported heterostructure perovskite-based photodetectors are listed in **Table 1**.[9–11,13–15,34,37,42,43]

It can be seen from Figure 3b,d that the responsivity and detectivity decrease with incident illumination power. This can be explained by the fact that the gain of a photodetector is calculated by $G = \frac{\tau}{t}$, where τ is the photocarrier lifetime and t is the carrier transit time. Since at a fixed bias the transit time is unchanged, the increase in photocarrier lifetime will lead to an increase in responsivity and detectivity. That is, at high incident power, the concentration of photocarriers is relatively higher and therefore there is greater probability for scattering and recombination. In contrast, at lower powers, the photocarrier concentration is lower and therefore there is relatively fewer

Adv. Mater. 2016,
DOI: 10.1002/adma.201603995

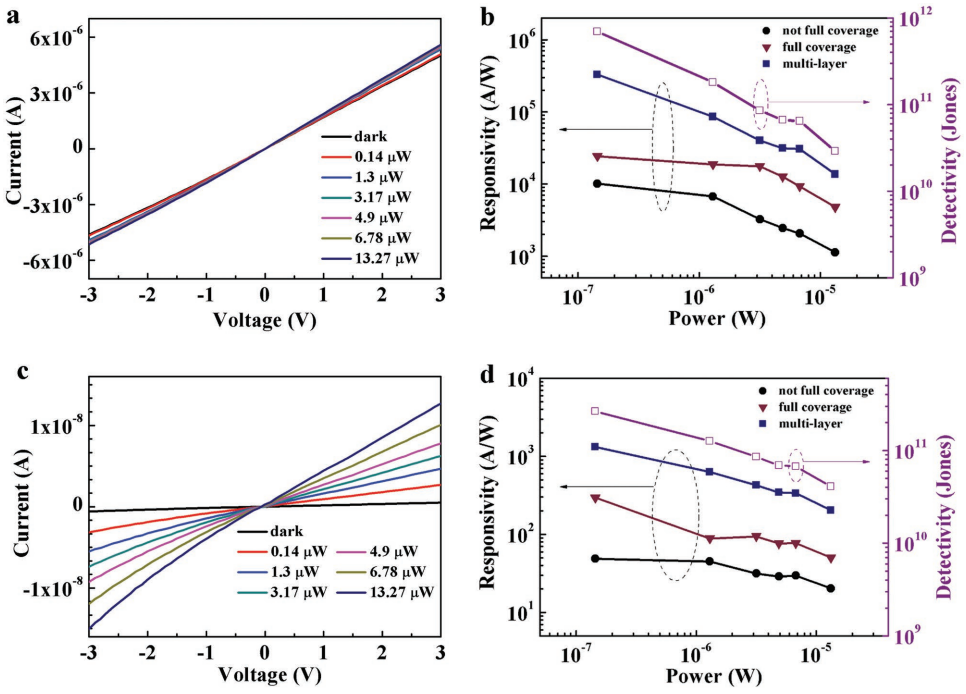

Figure 3. a) *I–V* plots of the thinnest 1T-MoS_2/$CH_3NH_3PbI_3$ under various illumination powers. b) Responsivities of 1T-MoS_2/$CH_3NH_3PbI_3$ photodetectors as a function of various illumination powers. c) *I–V* plot of the thinnest 2H-MoS_2/$CH_3NH_3PbI_3$ devices at different illumination power values. d) Responsivities of 2H-MoS_2/$CH_3NH_3PbI_3$ photodetectors as a function of various illumination powers.

scattering or recombination events and the gain values for the photodetector are higher.

Finally, the temporal photoresponse of the 1T-MoS_2/$CH_3NH_3PbI_3$ and 2H-MoS_2/$CH_3NH_3PbI_3$ photodetectors was tested under periodic illumination with an on/off interval of 4 s. The on/off switching behavior was preserved over multiple cycles. Current with respect to time is shown in **Figure 4**a,c for 1T and 2H phase devices, respectively. It is revealed that the photocurrents of both hybrid photodetectors are consistent and repeatable. The rise and decay time are defined as when the photocurrent and the dark current increase or decrease by 80% compared to their peak value.[33] The rise and decay times for the hybrid 1T-MoS_2/$CH_3NH_3PbI_3$ device were measured to be 0.45 and 0.75 s. In contrast, the 2H-MoS_2/$CH_3NH_3PbI_3$ device is faster by one order of magnitude. The rise time is less than 25 ms, which is the detection limit of our equipment, and the decay time is less than 50 ms, which is much faster than graphene-based perovskite photodetectors.[9,10,34] The difference in the rise and fall times between the 1T and 2H phase MoS_2 devices is determined by defects that act as recombination or generation centers. The fact that the 2H phase MoS_2 devices show faster response times is in contrast with the lower responsivity values reported in Figure 2. However, this can be reconciled by the fact that the 1T phase of MoS_2 is obtained by chemical exfoliation and is indeed more defective than the 2H phase material (see our previous

Table 1. Performance summary of reported heterostructure perovskite-based photodetectors.

Device structure	Incidence	Responsivity [A W^{-1}]	ON/OFF	Rise/fall	Detectivity [*J*]
MoS_2/$MAPbI_3$[13]	4.63pW @520 nm	2.12×10^4 @V_g = 20 V (V_g is the gate voltage)	≈10	10.7 s, 6.2 s	1.38×10^{10}
$MAPbI_3$/PDPP3T[42]	0.5 mW cm^{-2} @365 nm	10.7×10^{-3}	–	–	6.1×10^9
WS_2/$MAPbI_3$[14]	0.5 mW cm^{-2} @505 nm	17	1×10^5	2.7 ms, 7.5 ms	2×10^{12}
Graphene/$MAPbI_3$[11]	0.014 mW cm^{-2} @532 nm	223.5	<2	1.5 s	–
Graphene/$MAPbI_3$[37]	0.003 mW	115	<2	5.3 s	3×10^{12}
Graphene/$MAPbI_3$[10]	3.3 pW	2.6×10^6	–	55 s, 75 s	–
Graphene/$MAPbI_3$[9]	1 μW	180	<2	540 ms	1×10^9
Graphene/$MAPbBr_2I$[34]	1.052 nW	6×10^5	<2	750 ms	–
WSe_2/$MAPbI_3$[15]	–	110	10	2 s	2.2×10^{11}
TiO_2/$MAPbI_3$[43]	100 mW cm^{-2}	0.49×10^{-6}	70	0.02 s	–

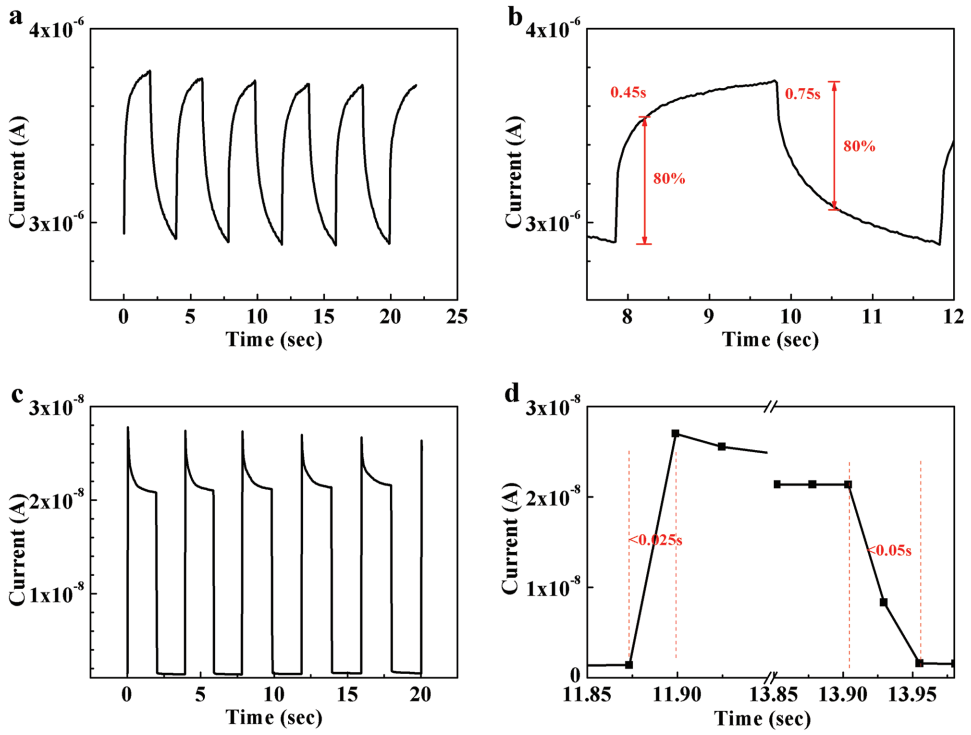

Figure 4. a) Photoswitching characteristics of 1T-MoS_2/$CH_3NH_3PbI_3$ photodetectors. b) Temporal voltage response of 1T-MoS_2/$CH_3NH_3PbI_3$ photodetectors. Measurements show a rise time of 0.45 s and a decay time of 0.75 s. c) Photoswitching characteristics of 2H-MoS_2/$CH_3NH_3PbI_3$ photodetectors. d) Temporal voltage response of 2H-MoS_2/$CH_3NH_3PbI_3$ photodetector with a rise time of 0.025 s and a decay time of 0.05 s.

work in refs. [19] and [20]). Annealing of 1T phase to obtain 2H phase allows relaxation of structural defects. The responsivity of 1T phase devices is higher because charge transfer is facilitated due to its metallic character as well as high density of defects—as indicated by more efficient PL quenching. However, the trapping of carriers by defects leads to lower response times for the 1T phase and the relative reduction in defect concentration leads to faster response times in the 2H phase MoS_2 devices.

In conclusion, we have investigated the optoelectronic properties of solution-processed hybrid photodetectors based on chemically exfoliated 2D MoS_2 nanosheets and organolead halide perovskites. We studied the influence of metallic and semiconducting phases of 2D MoS_2 on the performance of hybrid photodetectors. We found that it is possible to achieve exceptionally high photoresponsivity and EQE values for hybrid photodetectors consisting of 1T phase nanosheets integrated with perovskites. However, the metallic nature of the 1T phase leads to high dark currents, which in turn leads to impractical on/off ratios. In contrast, semiconducting 2H phase can mitigate the low on/off ratio while providing photoresponsivity and detectivity. Our work provides insights into how different phases of 2D materials can be utilized for photodetection to mitigate key challenges.

Experimental Section

Materials: All chemicals, unless stated otherwise, were purchased from Sigma-Aldrich without further purification.

Chemical Exfoliation of MoS_2: Chemically exfoliated MoS_2 was synthesized by lithium intercalation into bulk MoS_2 powder as reported previously.[19] Namely, 3 mL of 1.6 M *n*-butyllithium was added to 0.3 g of bulk MoS_2 powder under argon and refluxed for 48 h. The mixture was then filtered and washed with hexane to remove any excess of butyllithium or other organic residue. The intercalated powder was then exfoliated in water at 1.5 mg mL^{-1}, sonicated for 1 h, and centrifuged to remove lithium cations as well as the nonexfoliated bulk material.

Perovskite: CH_3NH_3I was synthesized by mixing 24 mL of methylamine with 10 mL of hydroiodic acid in a round-bottom flask at 0 °C for 2 h with stirring. The solvent was removed by heating the solution in a rotary evaporator at 50 °C. The white precipitate of raw CH_3NH_3I was washed with ethanol, filtered, and then washed with diethyl ether. This procedure was repeated three times. After the last filtration, the products were dried at 60 °C in a vacuum oven for 24 h and stored in a glove box. A 40 wt% solution of $CH_3NH_3PbI_3$ was prepared by dissolving PbI_2 and CH_3NH_3I in a 1:1 molar ratio in *N*,*N*-dimethylformamide and heating at 70 °C overnight inside an argon-filled glove box.

Device Fabrication: Silicon oxide on silicon substrates was sequentially cleaned in soapy water, deionized water, acetone, and ethanol in an ultrasonic bath for 15 min, and dried under nitrogen flow. Gold contacts were deposited on top of the substrates using thermal deposition with a shadow mask. MoS_2 films were prepared using vacuum filtration of chemically exfoliated nanosheets in water using a 25 nm membrane from Millipore, then transferred onto the target substrate. The thickness of the 1T MoS_2 film was varied depending on the volume of the MoS_2 solution filtered. The films can be converted to the 2H phase by annealing the as-exfoliated 1T MoS_2 film in argon at 300 °C for half an hour. The perovskite precursor was spin-coated at 3000 rpm for 60 s on the MoS_2 film. The substrates were then heated on a hot plate at 100 °C for 20 min. To improve the device stability in air, layers of polymethylmethacrylate (PMMA) were spin-coated onto the perovskite films at 4000 rpm for 60 s. Finally, the devices were heated on a hot plate at 80 °C for 10 min.

Adv. Mater. **2016**,
DOI: 10.1002/adma.201603995

Supporting Information

Supporting Information is available from the Wiley Online Library or from the author.

Acknowledgements

H.Z. would like to acknowledge financial support from the Shenzhen Science and Technology Innovation Committee (Grant Nos. KQCX20140522143114399 and JCYJ20160229122349365). JY, MC acknowledge support from the Rutgers Energy Institute. RF acknowledges support for Department of Education GAANN Fellowship.

Received: July 28, 2016
Revised: October 18, 2016
Published online:

[1] M. Chhowalla, H. S. Shin, G. Eda, L.-J. Li, K. P. Loh, H. Zhang, *Nat. Chem.* **2013**, *5*, 263.
[2] R. Lu, C. Christianson, B. Weintrub, J. Z. Wu, *ACS Appl. Mater. Interfaces* **2013**, *5*, 11703.
[3] G. Konstantatos, M. Badioli, L. Gaudreau, J. Osmond, M. Bernechea, F. P. G. de Arquer, F. Gatti, F. H. L. Koppens, *Nat. Nanotechnol.* **2012**, *7*, 363.
[4] F. H. L. Koppens, T. Mueller, P. Avouris, A. C. Ferrari, M. S. Vitiello, M. Polini, *Nat. Nanotechnol.* **2014**, *9*, 780.
[5] M. R. Esmaeili-Rad, S. Salahuddin, *Sci. Rep.* **2013**, *3*, 02345.
[6] S. H. Yu, Y. Lee, S. K. Jang, J. Kang, J. Jeon, C. Lee, J. Y. Lee, H. Kim, E. Hwang, S. Lee, J. H. Cho, *ACS Nano* **2014**, *8*, 8285.
[7] S. D. Stranks, G. E. Eperon, G. Grancini, C. Menelaou, M. J. P. Alcocer, T. Leijtens, L. M. Herz, A. Petrozza, H. J. Snaith, *Science* **2013**, *342*, 341.
[8] W. Nie, H. Tsai, R. Asadpour, J.-C. Blancon, A. J. Neukirch, G. Gupta, J. J. Crochet, M. Chhowalla, S. Tretiak, M. A. Alam, H.-L. Wang, A. D. Mohite, *Science* **2015**, *347*, 522.
[9] Y. Lee, J. Kwon, E. Hwang, C.-H. Ra, W. J. Yoo, J.-H. Ahn, J. H. Park, J. H. Cho, *Adv. Mater.* **2015**, *27*, 41.
[10] M. Spina, M. Lehmann, B. Náfrádi, L. Bernard, E. Bonvin, R. Gaál, A. Magrez, L. Forró, E. Horváth, *Small* **2015**, *11*, 4824.
[11] Z. Sun, L. Aigouy, Z. Chen, *Nanoscale* **2016**, *8*, 7377.
[12] M. He, Y. Chen, H. Liu, J. Wang, X. Fang, Z. Liang, *Chem. Commun.* **2015**, *51*, 9659.
[13] D.-H. Kang, S. R. Pae, J. Shim, G. Yoo, J. Jeon, J. W. Leem, J. S. Yu, S. Lee, B. Shin, J.-H. Park, *Adv. Mater.*, **2016**, *28*, 7799.
[14] C. Ma, Y. Shi, W. Hu, M.-H. Chiu, Z. Liu, A. Bera, F. Li, H. Wang, L.-J. Li, T. Wu, *Adv. Mater.* **2016**, *28*, 3683.
[15] J. Lu, A. Carvalho, H. Liu, S. X. Lim, A. H. Castro Neto, C. H. Sow, *Angew. Chem.* **2016**, *128*, 12124.
[16] O. Lopez-Sanchez, D. Lembke, M. Kayci, A. Radenovic, A. Kis, *Nat. Nanotechnol.* **2013**, *8*, 497.
[17] D.-H. Kang, M.-S. Kim, J. Shim, J. Jeon, H.-Y. Park, W.-S. Jung, H.-Y. Yu, C.-H. Pang, S. Lee, J.-H. Park, *Adv. Funct. Mater.* **2015**, *25*, 4219.
[18] Z. Yang, R. Grassi, M. Freitag, Y.-H. Lee, T. Low, W. Zhu, *Appl. Phys. Lett.* **2016**, *108*, 083104.
[19] G. Eda, H. Yamaguchi, D. Voiry, T. Fujita, M. Chen, M. Chhowalla, *Nano Lett.* **2011**, *11*, 5111.
[20] D. Voiry, M. Salehi, R. Silva, T. Fujita, M. Chen, T. Asefa, V. B. Shenoy, G. Eda, M. Chhowalla, *Nano Lett.* **2013**, *13*, 6222.
[21] M. Acerce, D. Voiry, M. Chhowalla, *Nat. Nanotechnol.* **2015**, *10*, 313.
[22] Y. Yao, Z. Lin, Z. Li, X. Song, K.-S. Moon, C. Wong, *J. Mater. Chem.* **2012**, *22*, 13494.
[23] Q. H. Wang, K. Kalantar-Zadeh, A. Kis, J. N. Coleman, M. S. Strano, *Nat. Nanotechnol.* **2012**, *7*, 699.
[24] L. Wang, Z. Xu, W. Wang, X. Bai, *J. Am. Chem. Soc.* **2014**, *136*, 6693.
[25] Y. Wang, Z. Xia, S. Du, F. Yuan, Z. Li, Z. Li, Q. Dai, H. Wang, S. Luo, S. Zhang, H. Zhou, *Nanotechnology* **2016**, *27*, 175201.
[26] K. Wang, J. Wang, J. Fan, M. Lotya, A. O'Neill, D. Fox, Y. Feng, X. Zhang, B. Jiang, Q. Zhao, H. Zhang, J. N. Coleman, L. Zhang, W. J. Blau, *ACS Nano* **2013**, *7*, 9260.
[27] S. De Wolf, J. Holovsky, S.-J. Moon, P. Löper, B. Niesen, M. Ledinsky, F.-J. Haug, J.-H. Yum, C. Ballif, *J. Phys. Chem. Lett.* **2014**, *5*, 1035.
[28] S. Jiménez Sandoval, D. Yang, R. F. Frindt, J. C. Irwin, *Phys. Rev. B* **1991**, *44*, 3955.
[29] P. Joensen, E. D. Crozier, N. Alberding, R. F. Frindt, *J. Phys. C: Solid State Phys.* **1987**, *20*, 4043.
[30] C. Wehrenfennig, M. Liu, H. J. Snaith, M. B. Johnston, L. M. Herz, *J. Phys. Chem. Lett.* **2014**, *5*, 1300.
[31] F. Deschler, M. Price, S. Pathak, L. E. Klintberg, D.-D. Jarausch, R. Higler, S. Hüttner, T. Leijtens, S. D. Stranks, H. J. Snaith, M. Atatüre, R. T. Phillips, R. H. Friend, *J. Phys. Chem. Lett.* **2014**, *5*, 1421.
[32] A. Capasso, F. Matteocci, L. Najafi, M. Prato, J. Buha, L. Cinà, V. Pellegrini, A. D. Carlo, F. Bonaccorso, *Adv. Energy Mater.* **2016**, *6*, 1600920.
[33] R. Kappera, D. Voiry, S. E. Yalcin, B. Branch, G. Gupta, A. D. Mohite, M. Chhowalla, *Nat. Mater.* **2014**, *13*, 1128.
[34] Y. Wang, Y. Zhang, Y. Lu, W. Xu, H. Mu, C. Chen, H. Qiao, J. Song, S. Li, B. Sun, Y.-B. Cheng, Q. Bao, *Adv. Opt. Mater.* **2015**, *3*, 1389.
[35] M. I. Saidaminov, V. Adinolfi, R. Comin, A. L. Abdelhady, W. Peng, I. Dursun, M. Yuan, S. Hoogland, E. H. Sargent, O. M. Bakr, *Nat. Commun.* **2015**, *6*, 8724.
[36] M. I. Saidaminov, M. A. Haque, M. Savoie, A. L. Abdelhady, N. Cho, I. Dursun, U. Buttner, E. Alarousu, T. Wu, O. M. Bakr, *Adv. Mater.* **2016**, *28*, 8144.
[37] V. Q. Dang, G.-S. Han, T. Q. Trung, L. T. Duy, Y.-U. Jin, B.-U. Hwang, H.-S. Jung, N.-E. Lee, *Carbon* **2016**, *105*, 353.
[38] Z. Yin, H. Lin, J. Lin, Y. Shi, Y. Sun, G. Lu, Q. Zhang, X. Chen, H. Zhang, *ACS Nano* **2012**, *6*, 74.
[39] Y. Zhang, J. Du, X. Wu, G. Zhang, Y. Chu, D. Liu, Y. Zhao, Z. Liang, J. Huang, *ACS Appl. Mater. Interfaces* **2015**, *7*, 21634.
[40] W. Wang, H. Xu, J. Cai, J. Zhu, C. Ni, F. Hong, Z. Fang, F. Xu, S. Cui, R. Xu, L. Wang, F. Xu, J. Huang, *Opt. Express* **2016**, *24*, 8411.
[41] Y. Guo, C. Liu, H. Tanaka, E. Nakamura, *J. Phys. Chem. Lett.* **2015**, *6*, 535.
[42] S. Chen, C. Teng, M. Zhang, Y. Li, D. Xie, G. Shi, *Adv. Mater.* **2016**, *28*, 5969.
[43] H.-R. Xia, J. Li, W.-T. Sun, L.-M. Peng, *Chem. Commun.* **2014**, *50*, 13695.